

Temperature and water measurements in flames using 1064 nm Laser-Induced Grating Spectroscopy (LIGS)

Francesca De Domenico*¹, Thibault F. Guiberti², Simone Hochgreb¹,
William L. Roberts², Gaetano Magnotti²

¹*University of Cambridge, Cambridge, United Kingdom*

²*King Abdullah University of Science and Technology (KAUST), CCRC, Thuwal
23955-6900, Saudi Arabia*

Abstract

Laser-Induced Grating Spectroscopy (LIGS) is applied to premixed CH₄/air laminar flat flames under operating pressures of 1 to 6 bar. For the first time, temperature and water concentration have been acquired simultaneously in a reacting flow environment using LIGS. A 1064 nm pulsed laser is used as pump to generate a temporary stationary intensity grating in the probe volume. Water molecules in the flame products absorb the laser energy and generate a thermal grating if sufficiently high energies are delivered by the laser pulses, here more than 100 mJ per pulse. Such energies allow the electric field to polarize the dielectric medium, resulting in a detectable electrostrictive grating as well. This creates LIGS signals containing both the electrostrictive and the thermal contributions. The local speed of sound is derived from the oscillation frequency of LIGS signals, which can be accurately measured from the single shot power spectrum. Data show that the ratio between the electrostrictive and the thermal peak intensities is an indicator of the local water concentration. The measured values of speed of sound, temperature, and water concentration in the flames examined compare favorably with flame simulations with Chemkin, showing an estimated accuracy of 0.5 to 2.5% and a precision of 1.4-2%. These results confirm the potential for 1064-nm LIGS-based thermometry for high-precision temperature measurements of combustion processes.

Keywords: Combustion diagnostics, thermometry, laser induced grating spectroscopy, elevated pressure

1. Introduction

Temperature is a key parameter in combustion and reacting flows as it affects engine efficiency, pollutant emissions, and noise. Accurate and precise measurements of gas temperature are desirable for model validation and for effective and fast design of low emission internal combustion engines and gas turbines. However, the hostile environment of a combustion chamber makes these measurements extremely challenging, so that only few experimental techniques are able to probe temperature without perturbing the flow. Laser diagnostics have repeatedly demonstrated their capability in non-intrusive investigation of temperature and other scalars. In this work, we demonstrate Laser-Induced Grating Spectroscopy (LIGS) as a promising technique to measure local temperature and water concentration in high pressure combustion environments.

There are a number of optical techniques that can be used for non-intrusive temperature measurements. Interferometry and laser absorption techniques are robust and can achieve good accuracy, but are limited to line of sight measurements [1, 2]. Raman and Rayleigh scattering are based on the elastic scattering of molecules, but they are characterized by relatively low signals in the case of Raman scattering, and severe interference from surfaces and particles, in the case of Rayleigh scattering [3, 4]. Multiple spectral line laser-induced fluorescence allows spatially resolved measurements of temperature, as long as a fluorescing species is either added or available, and a means of high temperature calibration is available for the particular species. A detailed knowledge of the composition is required to estimate the local quenching, so that quantitative measurements are challenging [5]. Finally, non-linear optical techniques such as Coherent Anti-Stokes Raman Spectroscopy (CARS) and LIGS offer space-resolved measurements and good signal to noise ratio because the signal output is in the form of a coherent laser beam that can be easily isolated from the background noise. CARS is an expensive technique, which typically requires high wavelength accuracy, high power pulses, delicate alignment capabilities, and high spectral resolution. CARS signals scale well with pressure ($\propto p^2$), but accurate temperature measurements at high pressure require complex modelling of the collisional broadening and knowledge of the composition [6, 7, 8, 9]. LIGS

*Corresponding author

Email address: fd314@cam.ac.uk (Francesca De Domenico*1)

demands a significantly simpler set-up and data analysis than CARS. It relies on the measurement of the modulation frequency of a laser-induced transient grating signal, which is related to the local speed of sound. Signals scale approximately with the square of the local density and thus they benefit from higher densities available at high pressure. The high potential of LIGS to measure gas properties such as temperature, pressure, velocity, and mixture concentration has been demonstrated in both reacting and non reacting flows [10, 11, 12, 13, 14, 15, 16, 17, 18]. LIGS signals can be generated either by a resonant or a non-resonant process in the interactions between the medium and the crossing laser beams. The non-resonant process arises from an electrostrictive interaction named Laser-Induced Electrostrictive Grating Scattering (LIEGS) whereas the resonant process arises from resonant absorption of the radiation energy, leading to Laser-Induced Thermal Grating Scattering (LITGS). In the presence of strongly absorbing molecules, the energies required to generate the thermal gratings are normally one order of magnitude lower than those needed to generate the electrostrictive gratings. Although LITGS typically offers a higher signal to noise ratio than LIEGS, its main limitation is the need for sufficient concentrations of a resonant species at the available pump laser wavelength.

In this work, LIGS (LIEGS + LITGS) measurements are performed in premixed CH₄/air laminar flat flames under operating pressures of 1 to 6 bar. A very accessible laser wavelength (1064 nm) from the popular Nd:YAG laser is used. A particular novelty of the development has been the demonstration of the technique without the use of an added absorber for flames at pressure. The first harmonic of the Nd:YAG laser at 1064 nm is ideal to achieve the high energy outputs required to yield LIEGS and also shows promise to produce LITGS using water as an absorber, which is available for free in combustion products. In addition, since the LITGS signal intensity is expected to depend on the water concentration while the LIEGS signal intensity does not, combined LITGS and LIEGS should allow measuring water concentration. Results show that 1064 nm LIGS is a non-intrusive, accurate, low cost technique to measure temperature and water concentration in combustors.

The paper is organized as follows: following a brief introduction on the LIGS technique (Sec. 2), the optical set-up and the experimental facilities are described (Sec. 3). The experimental procedure is then explained, with a particular focus on the effects of operating pressure and pump laser energy on the amplitude and oscillation frequency of the LIGS signals. Finally, the experimental results obtained for flames at a pressure of 4 bar are de-

scribed in more details and are compared with burner-stabilized, lean pre-mixed methane/oxygen/nitrogen flames at high pressure simulated using a chemical kinetic model. Comparisons are based on speed of sound, temperature and water concentration (Sec. 4).

2. LIGS technique

Laser Induced Grating Spectroscopy is akin to a four wave mixing technique based on opto-acoustic and acousto-optic effects arising from the interference of two pulsed laser beams [19]. In a typical LIGS experiment, two parallel, polarised, coherent pulsed pump laser beams from the same laser source are crossed at an angle θ to generate an interference pattern within the crossing volume, called a grating, of spacing Λ . The value of Λ is determined by the crossing angle and the laser wavelength λ :

$$\Lambda = \frac{\lambda/2}{\sin(\theta/2)} \quad (1)$$

The interaction between the medium and the radiation in the interference pattern generates both resonant and non-resonant processes. The non-resonant process arises from an electrostrictive interaction and leads to LIEGS, whereas the resonant process arises from resonant absorption of the radiation energy, leading the generation of a thermal grating, thus enabling LITGS. The electrostrictive interaction involves the polarizability of the molecules such that they are driven towards the regions of higher electric field intensity. The resulting pressure perturbation drives two oppositely propagating acoustic waves, which form a travelling density perturbation oscillating in time at a frequency determined by the transit time of the sound waves across the grating wavelength [19, 11, 20]. The resonant process requires that the wavelength of the incident pump light corresponds to a spectral absorption in some molecular species of the gas. Molecular excitation is higher in corresponding regions of high field intensity in the interference (grating) pattern. The absorbed energy is subsequently released by collisional quenching processes, resulting in localised perturbations to the temperature and density in the form of a thermal grating. The latter modulation is also accompanied by associated pressure and density waves, which interact periodically in and out of phase with the temperature grating, and can be detected as a locally varying field. The matter of which of the resonant or non-resonant processes dominates depends upon the properties of

the incoming light and of the species present in the interaction region. In strongly absorbing media (with respect to the pump laser wavelength used), the thermal grating process dominates, leading to LITGS signals which can usually be observed using relatively low energy pulses (1 to 10 mJ) [21]. Electrostrictive gratings do not require an absorbing species, and can be induced by non-resonant wavelengths, but since they are normally orders of magnitude weaker than the thermal gratings, much higher energy pulses (more than 100 mJ) are required to obtain detectable scattered signals [19, 21]. Although the LITGS technique offers significantly higher signal to noise ratio than LIEGS, its main limitation is the need for sufficient concentrations of a resonant species at the available wavelength. On the other hand, both techniques benefit from the higher densities available in experiments at higher pressures.

The signal generated in the probe volume is extracted by a coherent probe beam incident at the appropriate Bragg angle θ_B to the grating:

$$\theta_B = \sin^{-1} \frac{\lambda}{2\Lambda} \quad (2)$$

The Bragg-scattered light encodes the LIGS signal, which oscillates with the frequency modulating the grating density. As the propagating waves in the grating move at the local speed of sound a , the modulation frequency of the scattered signal is determined as:

$$f = n \frac{a}{\Lambda} = 2n \frac{a}{\lambda} \sin \frac{\theta}{2} \quad (3)$$

where the factor $n = 1$ for thermal gratings and $n = 2$ for electrostrictive gratings, depending on whether the process is adiabatic (electrostriction) or non adiabatic (thermalisation). The speed of sound is related to the local temperature and mixture bulk properties. Therefore, assuming an ideal gas equation of state, the local temperature can be obtained from the oscillation frequency of the LIGS signal, as:

$$a^2 = \frac{1}{n^2} f^2 \Lambda^2 = \frac{\gamma \mathcal{R} T}{W} = \frac{\gamma p}{\rho} \quad (4)$$

where γ is the ratio of specific heats, \mathcal{R} the universal gas constant, W the bulk molecular weight of the mixture, and p , T , and ρ the local pressure, temperature, and density, respectively. Equation 4 shows that the measured

frequency is proportional to the local speed of sound, and can therefore be related to temperature, pressure, or density. Further information about the pressure and local composition can be inferred from the contrast and the decay rate of the LIGS signals [16, 22], which might be useful to evaluate the contribution of temperature or composition variations in complex flows when the latter change simultaneously.

3. Experimental Set-up

3.1. Optical layout

The optical layout of the experiment is sketched in Fig. 1. A seeded pulsed Nd:YAG laser (Continuum Powerlite DLS9010) generates a laser beam with a wavelength $\lambda = 1064$ nm at a repetition rate of 10 Hz. The Q-switch delay is adjusted to deliver pulses of 12 ns duration with a total energy of 1 J. The pulse energy is then adjusted in the range from 75 to 350 mJ by manually rotating a half wave plate (HWP) placed before a polarizer beam splitter cube (PBSC). The beam level is raised to 1.20 m via a periscope tower to reach the height of the windows of the high-pressure vessel. Beyond the periscope, the beam has horizontal polarization.

A 50/50 beam splitter plate optimized for 1064 nm divides the beam into two identical beams. A delay line (DL) created by two mirrors on a translation stage is located in the path of one of the two beams to ensure that the two beams are in phase at the probe volume. The two parallel beams, separated by 50 mm, are crossed using a 75-mm diameter bi-convex crossing lens (CL) with a 750-mm focal length, resulting in a crossing angle $\theta \simeq 3.81^\circ$. This arrangement produces a grating of 16 μm spacing in a probe volume of length and width of approximately 5 mm and 200 μm , respectively. These dimensions are evaluated from calculations assuming a Gaussian beam waist with $M^2 = 2$, and the crossing beam geometry at the crossing point [10]. The continuous probe beam is generated by a continuous wave solid state laser (Coherent Verdi G) operating at 532 nm with a maximum power output of 17 W and a diameter of ~ 2 mm. A guide beam, also at 532 nm, produced by a diode laser (Thorlabs CPS532) is used as a tracer to identify the direction of the scattered signal and facilitate positioning of the collection optics. These four beams (two pump, the probe, and the tracer beams) are coplanar and alignment masks are used to adjust their respective positions. Details about the alignment procedure of the beams can be found in Appendix A. A dichroic harmonic beam splitter (Thorlabs HBSY12) reflects the LIGS signals (532

nm) and transmits the pump beams (1064 nm), which are then trapped in beam dumps (BD). The LIGS signals are re-collimated with a second 75-mm diameter bi-convex crossing lens (CL) with a 750-mm focal length, then travel for 1.5 m to reject spurious signals, and are finally collected by a PMT (Hamamatsu H10721-20, rise time: 0.57 ns). Two 550 nm low pass filters (T: 99.9% at 532 nm, T: 0.08% at 1064 nm) are mounted in front of the PMT to improve the rejection of spectral noise. The operation parameters of the PMT were selected to guarantee operation in the linear range.

An infrared photodiode (Thorlabs DET210) detects the pump pulses and triggers acquisition of the LIGS signals. The signals are recorded using an oscilloscope (Keysight DSOS804A, 10 Gs/s sampling rate, 8 GHz bandwidth).

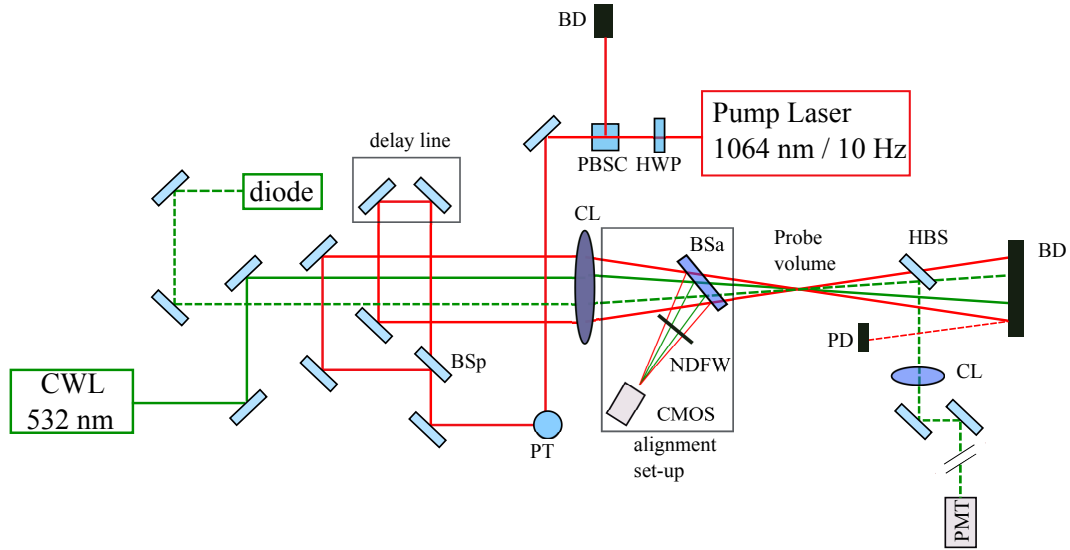


Figure 1: Optical layout of the experiment. Pump Laser: 1064 nm pulsed laser; CWL: Continuous Wavelength Laser; Diode: tracer beam; BSp: Beam Splitter (for 1064 nm); PT: Periscope Tower; CL: Crossing Lens; BD: Beam Dump; PBSC: Polarising Beam Splitter Cube; HWP: Half Wave Plate; BSa: Beam Sampler; NDFW: Neutral Density Filter Wheel; CMOS: CMOS Camera; HBS: Harmonic Beam Splitter (transmits 1064 nm and reflects 532 nm); PMT: Photomultiplier.

3.2. Experimental rig

LIGS measurements are performed in laminar premixed methane/air flat flames located in a vertically-oriented pressure vessel operated from 1 to 6

bar. This vessel is designed for continuous operation and features a $127 \times 127 \text{ mm}^2$ square cross-section chamber of 350 mm height. Resistance to pressure and temperature is achieved with 9-mm thick and air cooled stainless steel walls. Pressure is controlled with a manual needle valve and a dome-loaded back-pressure regulator (Equilibar GS2-NR-SS316) installed in parallel downstream of the exhaust port of the vessel. Pressure is first adjusted roughly by progressively closing the needle valve and fine adjustments are then made by tuning the back-pressure of the regulator using pressurized nitrogen. The vessel has four extension tubes mounted at 90 degrees to each other in the horizontal plane. These extension tubes terminate with 25.4-mm thick, 85-mm aperture diameter BK-7 windows (with a overall window diameter of 127 mm), providing optical access into the vessel. One window is used to pass the pump beams and the opposite window allows relaying the LIGS signals outside the vessel. The two remaining windows, mounted at 90 degrees, are used to monitor the flame. Jets of air continuously impinge on the four windows and prevent water from condensing on them. The flame is stabilized on a sintered-bronze porous plug burner (McKenna burner), which is water-cooled and has a diameter of 60 mm. A concentric porous ring that surrounds the porous plug can provide a steady co-flow of nitrogen or air but it was not used in these experiments because flame stability was impaired. The burner is mounted inside the vessel on a three-axis traverse system, which allows positioning the probe volume on the burner's center line, and at different heights above the porous surface. Flow-rates of methane and air are regulated using thermal mass-flow controllers (Brooks SLA series). These units are calibrated with air using gas flow calibrators (MesaLabs FlexCal series) prior to experiments to maintain an accuracy better than 1% for all conditions. The flame is ignited at atmospheric pressure by inserting a gas lighter through one of the side windows. The desired pressure set-point is then reached by slowly increasing pressure in the presence of the flame by using a co-flow of 80 slpm. The pressure is monitored by a pressure gauge (Omega Engineering) with a 0.25% accuracy. A S-type thermocouple (Pt/Rh) with a bead diameter of $d = 580 \text{ }\mu\text{m}$ is inserted in the vessel to measure the temperature of combustion products at the probe volume location for comparison with LIGS measurements.

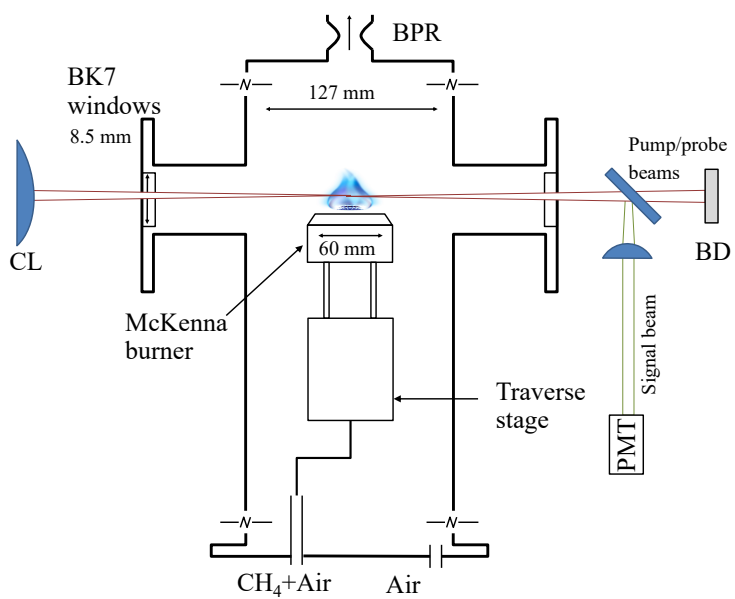


Figure 2: Schematic of the pressure vessel used in the experiments, including the McKenna burner inside the enclosure. CL: Crossing Lens; BPR: Back Pressure Regulator; BD: Beam Dump

4. Results and analysis

LIGS measurements were conducted in pressurized premixed methane/air flames using the 1064 nm Nd:YAG laser as pump. As a consequence, the signal obtained is the sum of contributions from the non-resonant (electrostrictive) process and the resonant (thermal) process due to the absorption of 1064 nm light by water molecules naturally present in combustion products. The LIGS signal oscillation frequency, and the corresponding speed of sound, are extracted from the power spectrum of the signal, while water concentration is obtained from the relative amplitude of the electrostrictive and thermal peaks. LIGS data is also compared to thermocouple measurements as well as simulations of burner-stabilized laminar premixed flames that include effects of conductive and radiative heat losses.

4.1. Signal description

Figure 3 shows two examples of ensemble-averaged LIGS signals acquired in the vessel: the blue dotted line is a signal in laboratory air at room temperature and atmospheric pressure inside the vessel, and the red solid line is a signal in a flame at 4 bar.

The pump laser pulse energy is set to 170 mJ and the probe power to 2 W. This combination of pump energy and probe power yields good signal to noise ratio and low standard deviations. The signal at room temperature and atmospheric pressure derives from electrostriction exclusively, because air molecules do not absorb radiation at the 1064 nm wavelength. The grid wavelength Λ of Eq. 4 is determined from this electrostrictive signal, for which the composition and temperature within the probe volume are known. A value of $\Lambda = 16 \mu\text{m}$ is found. The spacing Λ of the stationary grating is the same both in the air and in the flames, apart from the small distortion of the laser beams generated by the flame¹. The red solid line shows the signal acquired in the products of a nearly-stoichiometric flame (equivalence ratio of $\phi = 0.95$) at 4 bar. The water molecules in the flame products absorb the 1064 nm light only weakly: the absorption cross section of water molecules at 1064 nm is around two orders of magnitude smaller than that of common absorbers used for LITGS, such as toluene and acetone at 266 nm ($\sigma \simeq 10^{-24} \text{ cm}^2$ for water versus $\sigma \simeq 10^{-22} \text{ cm}^2$ for acetone [23, 24]). Thus, more energetic pump pulses are needed to generate a detectable thermal

¹This effect has been evaluated to be nearly negligible for the flames analysed.

grating in the flame. More than 100 mJ per pulse are required for water against 1-10 mJ for acetone and toluene in [25]. With such high energies, a non negligible electrostrictive grating is also generated, as can be observed in the first few nano-seconds of the signal. While the electrostrictive process is prompt, the thermal process is slower and the onset of the LITGS occurs after an induction period associated with thermalisation of the absorbed radiation [26], so that the two contributions are separated by a time delay. A closer look at the first oscillations of the signal (inset in Fig. 3) in the case of the flame shows that the electrostrictive contributions in air and in the flame yield a first peak within a few nanoseconds after the laser pulse (marked E) while the much larger thermal contribution in the flame signal appears after a longer time delay of roughly 15 ns (marked T).

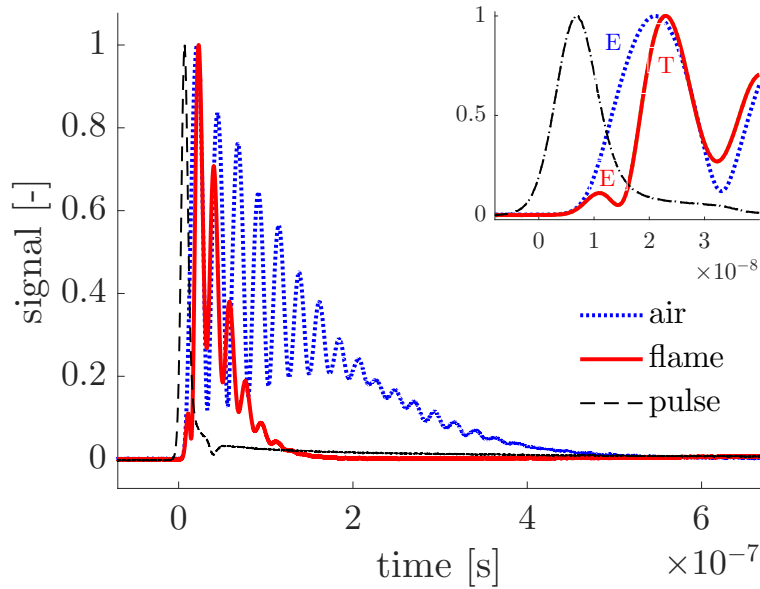


Figure 3: Normalized LIGS signals ensemble-averaged over 1000 shots. Electrostrictive signal acquired in air at room temperature and atmospheric pressure (blue dotted line) and thermal + electrostrictive signal in the products of a premixed CH_4/air flame with equivalence ratio $\phi = 0.95$ at 4 bar (red solid line). Black dashed-dotted line shows the pump laser pulse which triggers acquisition of the LIGS signals. Inset shows early times. Labels E and T refer to electrostrictive and thermal processes, respectively.

The top left panel of Fig. 4 shows a typical single-shot LIGS signal ac-

quired in the combustion products of the flame with $\phi = 0.95$ at 4 bar. Both contributions of the electrostrictive and thermal processes to the LIGS signal are clearly visible, but, as already noticed in Fig. 3, the amplitude of the thermal peak is much larger than the amplitude of the electrostrictive peak. The top right panel of Fig. 4 shows the power spectrum corresponding to this single-shot LIGS signal. In this power spectrum, only the peak associated with the thermal contribution can be clearly identified, with an oscillation frequency of $f_T = 53.3$ MHz. This suggests that, while a first peak is detectable, the electrostrictive process does not contribute significantly to the LIGS signal as a whole. This happens because the electrostrictive contribution is damped out within tens of nanoseconds. This effect has been reported earlier [20] and is due the cut-off frequency imposed by the laser pulse duration.

As shown in [20], if the LIGS oscillation frequency is higher than the laser pulse cutoff frequency, the diffraction efficiency of the grating decreases due to the destructive interference between the acoustic waves generated at different times during the long excitation pulse. The laser pulse duration used in this study is $\tau_L = 12$ ns, defining a system cut-off frequency of $f_{co} \simeq 1/\tau_L = 83$ MHz, which is smaller than the electrostrictive frequency of this signal $f_E = 2 \times f_T \simeq 106.6$ MHz. Thus, the electrostrictive signal decays immediately after the first peak is generated, and its contribution cannot be further identified in the power spectrum.

The bottom row of Fig. 4 shows the single-shot LIGS signal (left) and the corresponding power spectrum (right) for another flame at 4 bar that features a lower equivalence of $\phi = 0.60$. In this case, both contributions of the LIEGS and LITGS signals can be identified in the time (single-shot signal) and frequency (power spectrum) domains. This is attributed to the lower temperature experienced in this flame (due to a larger excess of air), which yields a smaller speed of sound and a smaller electrostrictive oscillation frequency of $f_E \simeq 78$ MHz $<$ $f_{co} = 83$ MHz. In this case, the electrostrictive oscillations do not dissipate immediately, and the overlap of thermal and electrostrictive oscillations can be observed in time trace. Depending on pressure and equivalence ratio, the relative contributions of the LIEGS and LITGS signals vary. However, it should be noted that such contributions can always be distinguished clearly at early times. In this case, the amplitude of the thermal and electrostrictive peaks are similar: less water is produced by the flame due to the lower equivalence ratio, and this decreases the peak amplitude of the thermal grating. Therefore, Fig. 4 shows that the

ratio between the intensity of the first thermal (I_T) and electrostrictive (I_E) peaks is a function of the equivalence ratio. This ratio, $R_W = I_T/I_E$, has a value $R_W = 8.3$ for the example with $\phi = 0.95$, and a much smaller value, $R_W = 1.2$, for $\phi = 0.60$. Since the LITGS signal intensity is expected to be proportional to the water concentration, while the LIEGS signal intensity does not, the ratio R_W can provide a measure of the water concentration. Following this argument, the LIGS signals shown in Fig. 4 suggest that the water concentration is much larger in the products of the flame with $\phi = 0.95$ than that with $\phi = 0.60$. This is the expected result based on simple equilibrium calculations.

4.1.1. Calibration from reference conditions

Let $f_{E,0}$ be the electrostriction frequency in air and a_0 the corresponding speed of sound at room temperature T_0 used for calibration. The LIGS oscillation frequency in flames $f_{T,f}$ (taken here equal to that of the LITGS contribution f_T in the power spectrum of Fig. 4) is extracted from the power spectrum of the signals. Extracting the LIGS frequency from the power spectrum (regardless of whether the signal is thermal or electrostrictive) is more accurate than using the peaks and troughs in the time traces to evaluate the oscillation period, and, consequently, the oscillation frequency. From Eq. 4, assuming a negligible distortion of the beams due to the flame, the corresponding speed of sound a_f was obtained as:

$$a_f = 2 \frac{f_{T,f}}{f_{E,0}} a_0 \quad (5)$$

The factor of 2 arises from the electrostriction index. Eq. 5 shows that the accuracy of the technique relies on the accuracy in the knowledge of the speed of sound during calibration. Using a perfect gas equation and Eq. 5, the temperature in the combustion products T_f is determined as:

$$T_f = 4 \frac{f_{T,f}^2}{f_{E,0}^2} \frac{\gamma_0}{\gamma_f} \frac{W_f}{W_0} T_0 \quad (6)$$

where W_0 and W_f stand for the air and combustion products molar mass, respectively.

Figure 4 illustrates how the LITGS oscillation frequency $f_{T,f}$ can be accurately extracted from the power spectrum of the flame signals, without relying on complex fitting algorithms. However, Eq. 6 shows that inferring

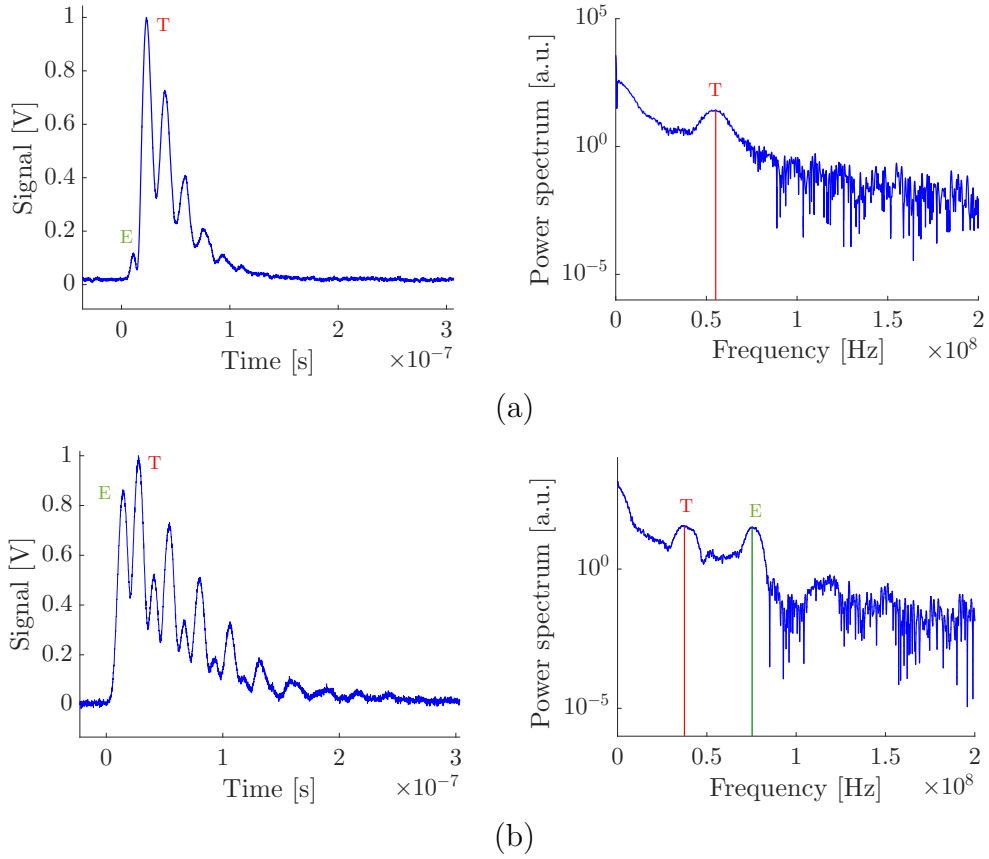


Figure 4: Sample LIGS single shots acquired in the 4 bar flame. Time trace (left) and power spectrum (right). Nearly-stoichiometric flame, $\phi = 0.95$, 5 mm above the surface of the burner (a) and lean flame, $\phi = 0.60$, 10 mm above the surface of the burner (b). The vertical red and green lines in the spectrum indicate the peaks for thermalisation (T) and electrostriction (E) (in the time and in the frequency domains).

the combustion product temperature requires the knowledge of the combustion product molar mass, which is *a priori* unknown. Normally, molar mass and specific heat capacity ratio are extracted from flame simulations. The hybrid thermal-electrostrictive LIGS technique, reported here for the first time, may allow to reduce uncertainties in determining the local composition by providing a relative measure of the water concentration. Indeed, the experimentally determined water concentration extracted from LIGS signals could be compared to simulated values to validate or improve the predictions on the local composition. Details on how this is achieved are shown in Sec. 4.4.1.

4.2. Pressure effects

Figure 5 shows LIGS signals acquired in combustion products for a fixed equivalence ratio $\phi = 0.95$ and at different pressures.

At atmospheric pressure, the LIGS signal has low amplitude and decays promptly. As the pressure increases, the signal amplitude and the number of peaks increase. Indeed, [20] showed that the signal intensity, I , and the rate of decay of the peak intensities, Γ , are both a function of the mixture density, ρ , as follows:

$$I \propto \rho^2 = \left(\frac{PW}{RT} \right)^2 ; \quad \Gamma \propto \frac{1}{\rho} = \frac{RT}{PW} \quad (7)$$

thus increased densities lead to higher signal amplitudes and lower decay rates, both of which are desirable for robust LIGS measurements. In the product region of flames, the signals at ambient pressure have a low amplitude and decay almost immediately, due to the high temperature and low density. On the other hand, at higher pressures, effects of beam steering due the density and temperature gradients are more pronounced. This could have a detrimental effect on spatial resolution. Various techniques have been suggested to mitigate the issue, such as enlarging one of the two pump beams to obtain an elliptically-shaped beam, which provides a more robust overlap despite the steering caused by the flame [9]. This technique has not been implemented here because only laminar flames are examined and temporal fluctuations of density are small, limiting beam steering.

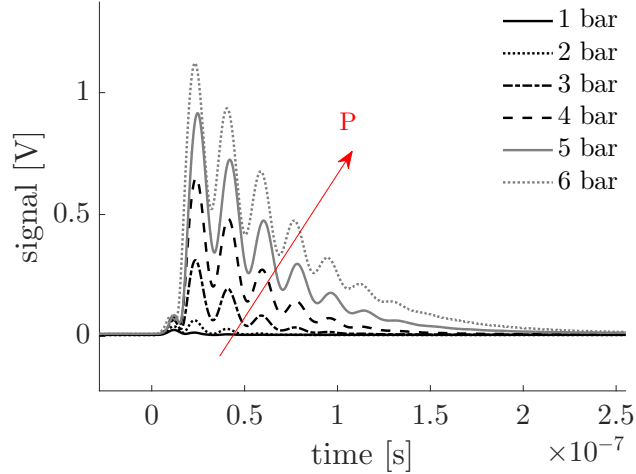


Figure 5: Ensemble-averaged LIGS signals acquired in the products of nearly stoichiometric flames ($\phi = 0.95$) at different pressures, 5 mm above the surface of the burner.

4.3. Pump energy effects

Figure 6 (left) shows ensemble-averaged LIGS signals acquired for pump pulse energies ranging from 75 mJ to 350 mJ. A larger pump laser irradiance (*e.g.* energy per unit time per unit area) yields LIGS signals of larger amplitude owing to the stronger thermal grating generated.

However, the measured LIGS oscillation frequency remains constant for the different energies considered (Fig. 6 (right)), indicating that the gas mixture within the probe volume is not being significantly heated due to the energy delivered by the pump beams. For thermal LIGS, this test is needed to verify the non-intrusiveness of the technique [27]. A large absorption cross section of the resonant molecule typically increases the risk of introducing excessive thermal energy to the probe volume. Because the absorption cross section of water at 1064 nm is not large, this effect is less likely to occur, and this is confirmed by Fig. 6 (right). The same figure shows that the standard deviation (thus the precision) of the measurements does not change for energies higher than 125 mJ, thus it is optimal to operate using energies in the range 125-350 mJ for the current optical set-up.

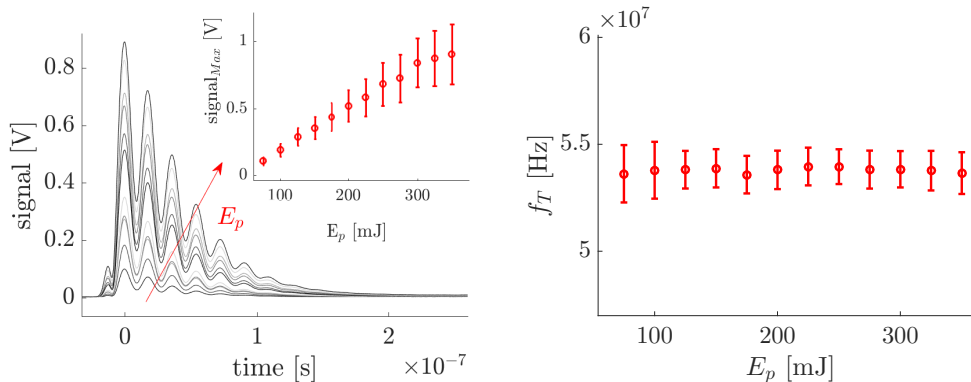


Figure 6: Ensemble-averaged LIGS signals acquired in the products of a nearly stoichiometric flame ($\phi = 0.95$) for a pressure of 4 bar and increasing pump pulse energies from 75 to 350 mJ. Inset shows the average signal amplitude for each pump energy level. Error bars represent plus/minus one standard deviation in the measurements (left). Measured LIGS oscillation frequency as a function of pump energy (right).

4.4. Measurements in flames at 4 bar

4.4.1. Speed of sound measurements

LIGS was used to determine the local speed of sound, water concentration, and temperature in the products of lean-to-rich premixed methane-air flames at 4 bar. The measurements shown here were conducted 5 mm above the surface of the burner, in the product zone. The equivalence ratio was varied from $\phi = 0.73$ to $\phi = 1.30$ by varying the fuel mass flow rate while keeping the air mass flow rate constant. For each flame, 1000 LIGS shots were acquired. The pump laser pulse energy was set to 170 mJ and the probe power to 2 W. Figure 7a compares the speed of sound inferred from LIGS measurements (based on Eq. 5) with predictions obtained with stabilised flame simulations.

The premixed flame species and temperature are modeled using the Chemkin software suite [28] using the burner-stabilized flame module with gas radiation, which accounts for heat losses to the surroundings. The required boundary conditions are the fresh reactant mass flow rate (which is prescribed in the experiments and, therefore, known) and the porous surface temperature (which was measured with a thermocouple). The GRI MECH 3.0 [29] detailed chemistry mechanism (specifically the C2-NO_x chemistry mechanism) was used to define chemical reactions and reaction rates, thermodynamic properties, and transport properties because it is known to perform well

for methane fuel over wide ranges of equivalence ratio and pressure. The radiation heat loss to the environment from gas products in the flame and post-flame region is also included using the radiation heat-transfer model and an optically-thin limit for both gas and dispersed phase [30]. The molecular weight used to determine the temperature from the speed of sound corresponds to those calculated in the product region of the flame, in the region where heat losses are still insignificant, as determined above. Nevertheless, in general, a potentially better route for model validation is to directly compare sound speeds obtained from LIGS rather than temperatures. The error bars in Fig. 7 represent plus/minus one standard deviation (σ_a) in the measurements. The precision of the measurements, evaluated as σ_a/\bar{a} is 1.4-1.7%. The agreement between simulations and experiments is very good at rich equivalence ratios, with discrepancies limited to 0.5%. For lean flames, the measured speed of sound is larger than the calculated speed of sound by up to 2.5%. A similar mismatch between experiments and simulations has been reported in [31] for lean flames at atmospheric pressure, also stabilized with a McKenna burner and using a data fitting algorithm to post-process LITGS signals in the time domain. The mismatch may therefore be inherent to inaccuracies of the simulations.

4.4.2. Temperature measurements

Figure 8 shows the temperature of the combustion products derived from the oscillation frequency measurements using Eq. 6. The mixture values of specific heat capacity ratio γ and molecular mass W of the flame products are extracted from the outputs of the burner-stabilised flame Chemkin simulations. Good agreement is obtained between experiments and simulations for nearly stoichiometric and rich conditions. For lean flames, the measured values are larger than the simulated ones by about 4.5%, echoing the mismatch observed in the speed of sound. To further investigate this mismatch, additional thermocouple measurements were made using a S-type thermocouple in a separate experiment in which LIGS was not activated and the thermocouple bead was placed at the exact same location as the LIGS the probe volume. The temperatures measured by the thermocouple (TC) are considerably lower than the measured LIGS and simulated Chemkin values and this is due to large radiative heat losses occurring at the bead of the thermocouple. The radiative heat losses can be corrected for, but the accuracy of the correction depends on the accuracy of the heat exchange model used [32]. Due to the complexity of the inner geometry of the vessel, as well

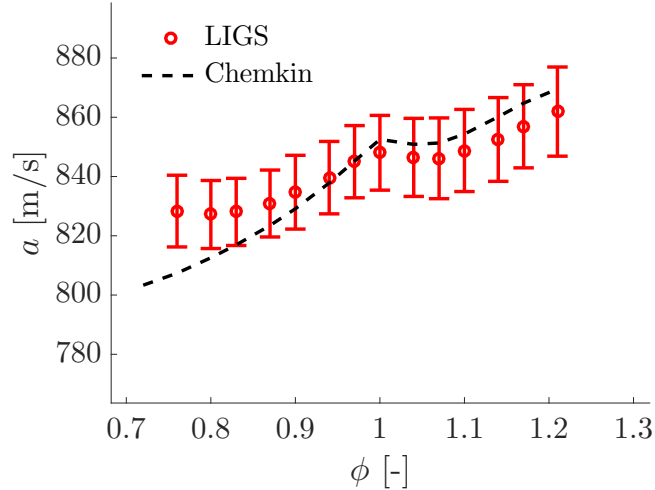


Figure 7: Speed of sound a as a function of equivalence ratio ϕ for flames at 4 bar. Dashed lines show calculated values of speed of sound from stabilised flame simulations using Chemkin. Error bars represent plus/minus one standard deviation in the measurements.

as the difficulties in defining the emissivity of the various surfaces and their temperature, it is only possible to provide an interval of confidence within which the actual combustion products temperature is expected to be. This interval is confined by an upper (TC h, dashed-dotted line) and a lower limit (TC l, dotted line), which are calculated by considering two extreme scenarios. The higher limit refers to a condition where the thermocouple is modeled as a small sphere in a cold vessel, without accounting for the proximity of the burner surface. For the lower limit, the burner surface is included in the heat exchange model. These two limits define an interval of approximately 100 K that brackets the LIGS measured and simulated temperatures. Although uncertainties in the thermocouple measurements, the slope of the temperature profile from thermocouple at low equivalence ratio matches better the LIGS output than the Chemkin simulations, further lending evidence for the possibility that the Chemkin model might be inadequate at lower equivalence ratio. The comparison offers further proof that the LIGS configuration used in this study allows measuring accurately the temperature in the products of lean-to-rich premixed flames at a pressure of 4 bar.

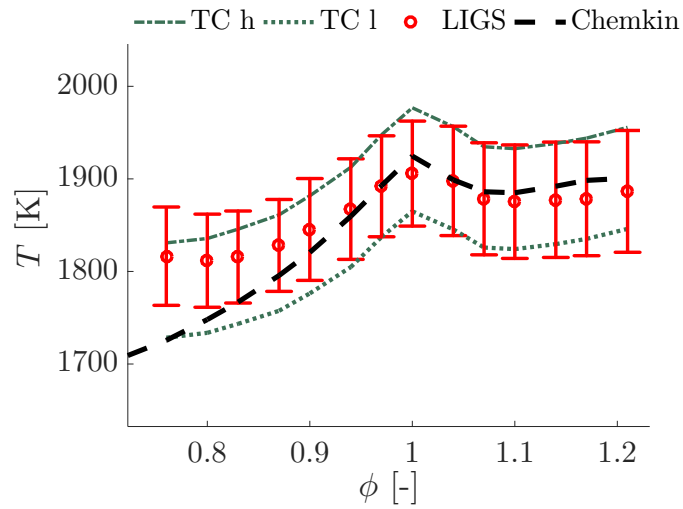


Figure 8: Temperature of the combustion products measured 5 mm above the burner surface as a function of the equivalence ratio for flames at 4 bar. LIGS measurements (red circles), Chemkin simulations (dashed line), thermocouple measurements corrected for radiative heat losses: lower limit (dotted line) and upper limit (dashed-dotted line).

4.4.3. Water concentration measurements

Figure 9 demonstrates a suggested calibration procedure to obtain water concentrations from the ratio of the thermalisation first peak amplitude I_T to the electrostriction first peak amplitude I_E . The amplitude (in volts) of the first electrostrictive LIEGS peak, I_E , is proportional to the pump energy E_p while the amplitude of the first thermal LITGS peak, I_T , is proportional to the product of the pump energy and the mole fraction of water, $E_p X_w$. Therefore, the ratio I_T/I_E is expected to be linearly proportional to the water mole fraction ($I_T/I_E \propto X_w$) but, as this value is set-up dependent, it requires calibration. A linear correlation between the peak amplitude ratio and the water concentration is demonstrated in Fig. 9 (left), where the experimentally determined ratio I_T/I_E is plotted against the water concentration X_W obtained from Chemkin simulations:

$$\frac{I_T}{I_E} = \alpha X_W + \beta \quad (8)$$

For this set-up and experimental data, the values $\alpha = 120.2$ and $\beta = -14.1$ are obtained from the experimental data in Fig. 9 (left) using a least squares linear fitting, determining the interpolation line. Using these values α and β , the local value X_W can be extracted from the ratio I_T/I_E for any LIGS signals, and Eq. 8. Figure 9 (right) compares the experimentally determined X_W with the output of Chemkin simulations for each equivalence ratio ϕ . Agreement between measurements and simulations is good, confirming that the hybrid LIGS configuration used in this study allows the accurate measurement of water mole fractions in the products of lean-to-rich premixed flames at a pressure of 4 bar, as long as the set-up dependent calibration data is provided. Experimentally determined water mole fractions in the probe volume can be used to verify the predicted values from flame simulations and improve the overall accuracy of LIGS by confirming the mixture composition. A correlation between the relative amplitude of the thermal and electrostrictive peaks and the absorber concentration was first shown for a propane - air non-reacting mixture in [16]. We demonstrate here for the first time the applicability of such method in reacting flows and at elevated pressure.

4.5. Comments and outlook

This work shows that LIGS using the widely available 1064 nm wavelength is a versatile and robust technique to detect the local speed of sound,

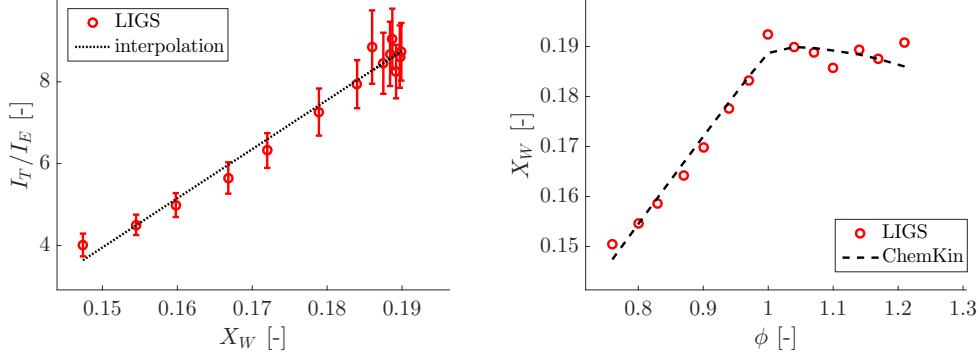


Figure 9: Relationship between water concentration X_W and thermal-to-electrostrictive peak intensity ratio I_T/I_E for flames at 4 bar (markers). Dotted line shows the linear interpolation of the data (left). Water concentration versus equivalence ratio: experimentally derived from LIGS measurements (markers) and calculated using Chemkin simulations (dashed line) (right).

temperature, and composition in a pressurized combustion environment containing a weak absorber such as water: no external tracer needs to be seeded into the flow to generate the thermal grating because water is a natural combustion product. Cold reactants (electrostriction) and hot product regions (electrostriction and thermalisation) can be probed using the same laser source at the same energy level. In addition, previous experiments have shown that soot particles, acting as a black body, can also absorb 1064 nm laser light and generate a thermal grating [22]. Thus seeding-free thermal LIGS measurements may be performed both in sooty and non-sooty flames, making hybrid LIGS a suitable candidate to probe reacting flows in hostile environments.

5. Conclusion

In this work, LIEGS and LITGS measurements using 1064 nm pump wavelengths have been demonstrated in laminar premixed CH_4/air flames at elevated pressure. We show that for moderate pulse energies (around 100 mJ/pulse), the LIGS signal consists of a combination of effects from the electrostrictive and the thermal contributions associated with low absorption by water molecules. At atmospheric conditions, the high temperature in the flames causes a nearly immediate dissipation of the transient grating,

so that the LIGS signals acquired at 1 bar have a low amplitude and are insufficient to clearly identify the oscillation frequency. At increased pressures, the density of the gas in the probe volume increases and sufficiently strong signals are generated. For pressures larger than 3 bar, LIGS signals have a large enough number of oscillations and good signal-to-noise ratio to clearly allow measurements of their oscillation frequency. Experiments conducted in combustion products of different equivalence ratios at 4 bar showed that the ratio between electrostrictive and thermal peaks is related to the water concentration in the probe volume. For the first time, temperature and water concentration measurements are obtained simultaneously from LIGS signals in pressurized flames. The experimentally determined values of speed of sound, temperature, and water concentration are shown to compare well with the simulated values using Chemkin. This work demonstrates that 1064-nm LIGS is a suitable and versatile technique to perform temperature and composition measurements in high pressure/high temperature reacting flows. As water is a common product of flames, this technique is particularly suitable to diagnose flames of industrial interest, as it does not require the addition of any absorbers to the flow, and it is significantly simpler than CARS. In summary, the work opens up the possibility of temperature and water measurements in regions of challenging optical access, such as high pressure and soot-containing regions in gas turbines, engine combustion chambers and reactors by using inexpensive light sources and optics.

6. Acknowledgment

The research reported in this publication was supported by funding from King Abdullah University of Science and Technology (KAUST). Francesca De Domenico's internship at KAUST University was fully funded by the KAUST Visiting Students Program. Francesca De Domenico is supported by the Honorary Vice-Chancellor's Award and a Qualcomm/ DTA Studentship (University of Cambridge). The authors are grateful to Dr. Benjamin A. O. Williams and Prof. Paul Ewart for valuable advice, developed under a previous EPSRC project EP/K02924X. The help of Anthony Bennet with the pressure vessel was highly appreciated.

Appendix A: Alignment procedure

A significant issue in obtaining successful LIGS signal is proper alignment. Here we describe the alignment procedure used to adjust and fine-tune the



Figure .10: Stationary grating generated by the pump beams imaged by the CMOS camera. Grid spacing is approximately $\Lambda = 16 \mu\text{m}$.

overlap of the four beams at the crossing point. As a first step, the two 1064 nm beams are synchronised in time using the delay line. The two beams are monitored at the crossing lens location using two coplanar photodiodes, whose outputs are recorded on the oscilloscope. The coherence of the two beams affects the amplitude of the signals, so it is important to minimise the phase shift between the two pulses, especially for multimode beams, which have a smaller coherence length [20].

Beyond the bi-convex lens, the crossing point of the four beams (the two 1064 nm pump beams and the two 532 nm beams) has to be adjusted: due to the chromatism of the lens, beams of different wavelengths cross at different axial locations. A pinhole ($50 \mu\text{m}$) on a two-axis manual traverse stage is positioned at the crossing location of the two 1064 nm pump beams. Then, the far field mirrors of the two 532 nm beams (probe and tracer) are adjusted until these two beams also pass through the pinhole. To fine-tune the overlap of the beams, the probe volume is imaged using a system of mirrors, lenses and filters (box in Fig. 1). A 10:90 reflection/transmission beam sampler (BSa) attached to a magnetic base is inserted in the path of the four beams, right before the probe volume, to mirror the crossing point while reducing the intensity of the beams. The sampled beams are further attenuated using

a neutral density filter wheel (NDFW). The reflected probe volume is then enlarged via a telescope (Edmund Optics-10 X) and imaged using a CMOS Camera (Thorlabs DCC1545M) connected to the computer. This procedure allows the fine adjustment of the overlap of the beams while imaging them. An image of the stationary grating generated from the overlap of the two pump beams is shown in Fig. .10. The stationary grating structure with the intensity fringes can clearly be observed. This alignment procedure has several advantages: firstly, it is easy to verify if the beams cross at their waist to improve the spatial resolution. Secondly, this arrangement allows verification of the overlap of the beams before starting any new experiments, and to correct for small misalignments during measurement campaigns: the mirror on the magnetic base can be easily removed before the beginning of the experiment.

References

- [1] A. C. Eckbreth, T. J. Anderson, Simultaneous rotational coherent anti-Stokes Raman spectroscopy and coherent Stokes Raman spectroscopy with arbitrary pump-Stokes spectral separation, *Optics Letters* 11 (8) (1986) 496–498.
- [2] R. K. Hanson, D. F. Davidson, Recent advances in laser absorption and shock tube methods for studies of combustion chemistry, *Progress in Energy and Combustion Science* 44 (2014) 103–114.
- [3] I. Lewis, E. Howell, *Handbook of Raman Spectroscopy: From the Research Laboratory to the Process Line*, CRC Press, 2001.
- [4] R. Dibble, R. Hollenbach, Laser Rayleigh Thermometry in Turbulent Flames, *Symposium (international) in Combustion* 18 (1) (1981) 1489–1499.
- [5] J. W. Daily, Laser induced fluorescence spectroscopy in flames, *Progress in Energy and Combustion Science* 23 (2) (1997) 133–199.
- [6] R. P. Lucht, Three-laser coherent anti-Stokes Raman scattering measurements of two species., *Optics letters* 12 (2) (1987) 78–80.
- [7] R. D. Hancock, F. R. Schauer, R. P. Lucht, R. L. Farrow, Dual-pump coherent anti-Stokes Raman scattering measurements of nitrogen and

- oxygen in a laminar jet diffusion flame, *Applied Optics* 36 (15) (1997) 3217–3226.
- [8] S. Roy, J. R. Gord, A. K. Patnaik, Recent advances in coherent anti-Stokes Raman scattering spectroscopy : Fundamental developments and applications in reacting flows, *Progress in Energy and Combustion Science* 36 (2) (2010) 280–306.
- [9] G. Magnotti, A. D. Cutler, P. M. Danehy, Beam shaping for CARS measurements in turbulent environments., *Applied optics* 51 (20) (2012) 4730–41.
- [10] H. Eichler, P. Gunter, D. Pohl, *Laser-Induced Dynamic Gratings*, Springer Berlin Heidelberg, 1986.
- [11] E. B. Cummings, I. A. Leyva, H. G. Hornung, Laser-induced thermal acoustics (LITA) signals from finite beams, *Applied Optics* 34 (18) (1995) 3290–3302.
- [12] H. Latzel, A. Dreizler, T. Dreier, J. Heinze, M. Dillmann, W. Stricker, G. M. Lloyd, P. Ewart, Thermal grating and broadband degenerate four-wave mixing spectroscopy of OH in high-pressure flames, *Applied Physics B* 673 (1998) 667–673.
- [13] D. J. W. Walker, R. B. Williams, P. Ewart, Thermal grating velocimetry, *Optics Letters* 23 (16) (1998) 1316–1318.
- [14] R. Stevens, P. Ewart, Single-shot measurement of temperature and pressure using laser-induced thermal gratings with a long probe pulse, *Applied Physics B* 117 (2004) 111–117.
- [15] B. Williams, M. Edwards, R. Stone, J. Williams, P. Ewart, High precision in-cylinder gas thermometry using Laser Induced Gratings: Quantitative measurement of evaporative cooling with gasoline/alcohol blends in a GDI optical engine, *Combustion and Flame* 161 (1) (2014) 270–279.
- [16] J. Kiefer, D. N. Kozlov, T. Seeger, A. Leipertz, Local fuel concentration measurements for mixture formation diagnostics using diffraction by laser-induced gratings in comparison to spontaneous Raman scattering, *Journal of Raman Spectroscopy* 39 (2008) 711–721.

- [17] A. Hell, F. J. Förster, B. Weigand, Validation of laser-induced thermal acoustics for chemically reacting H₂/air free jets, *Journal of Raman Spectroscopy* 47 (9) (2016) 1157–1166.
- [18] A.-I. Sahlberg, D. Hot, J. Kiefer, M. Aldén, Mid-infrared laser-induced thermal grating spectroscopy in flames, *Proceedings of the Combustion Institute* 36 (3) (2017) 4515–4523.
- [19] E. B. Cummings, Laser-induced thermal acoustics : simple accurate gas measurements, *Optics Letter* 19 (17) (1994) 1361–1363.
- [20] A. Stampanoni-Panariello, D. N. Kozlov, P. P. Radi, B. Hemmerling, Gas phase diagnostics by laser-induced gratings I . theory, *Applied Physics B* 111 (2005) 101–111.
- [21] T. Sander, P. Altenhöfer, C. Mundt, Development of Laser-Induced Grating Spectroscopy for Application in Shock Tunnels, *Journal of Thermophysics and Heat Transfer* 28 (1) (2014) 27–31.
- [22] M. S. Brown, W. L. Roberts, Single-Point Thermometry in High-Pressure, Sooting, Premixed Combustion Environments, *Journal of Propulsion and Power* 15 (1) (1999) 119–127.
- [23] M. Chaplin, [Water Absorption Spectrum \(2018-09-23\)](http://www1.lsbu.ac.uk/water/water_vibrational_spectrum.html).
URL http://www1.lsbu.ac.uk/water/water_vibrational_spectrum.html
- [24] M. C. Thurber, F. Grisch, B. J. Kirby, M. Votsmeier, R. K. Hanson, Measurements and modeling of acetone laser-induced fluorescence with implications for temperature-imaging diagnostics, *Applied optics* 37 (21) (1998) 4963–4978.
- [25] B. Williams, P. Ewart, Photophysical effects on laser induced grating spectroscopy of toluene and acetone, *Chemical Physics Letters* 546 (2012) 40–46.
- [26] P. H. Paul, R. L. Farrow, P. M. Danehy, Gas-phase thermal contributions to four-wave mixing, *Journal of the Optical Society of America* 12 (3) (1995) 384–392.

- [27] A. Hayakawa, T. Yamagami, K. Takeuchi, Y. Higuchi, T. Kudo, S. Lowe, Y. Gao, S. Hochgreb, H. Kobayashi, Quantitative measurement of temperature in oxygen enriched CH₄/O₂/N₂premixed flames using Laser Induced Thermal Grating Spectroscopy (LITGS) up to 1.0 MPa, Proceedings of the Combustion Institute 000 (2018) 1–8.
- [28] Chemkin Pro 18.2 (Reaction Design) (2018).
- [29] G. P. Smith, D. M. Golden, M. Frenklach, N. W. Moriarty, B. Eiteneer, M. Goldenberg, C. T. Bowman, R. K. Hanson, S. Song, W. C. Gardiner, V. V. Lissianski, Z. Qin, **GRI MECH 3.0**.
URL http://www.me.berkeley.edu/gri{}_mech/
- [30] D. D. Thomsen, F. F. Kuligowski, N. M. Laurendeau, Modeling of NO formation in premixed, high-pressure methane flames, Combustion and Flame 119 (3) (1999) 307–318.
- [31] A. Hell, F. Förster, E. Rosenko, B. Weigand, Experiments in chemically reacting subsonic flames and heated supersonic flows using Laser-Induced Thermal Acoustics (LITA), in: 16th Int Symp on Applications of Laser Techniques to Fluid Mechanics, Lisbon, Portugal, 09-12 July, 2012, 2012, pp. 1–11.
- [32] R. Lemaire, S. Menanteau, Assessment of radiation correction methods for bare bead thermocouples in a combustion environment, International Journal of Thermal Sciences 122 (2017) 186–200.